Journal of Materials Science & Technology 205 (2025) 42–52

Contents lists available at ScienceDirect

Journal of Materials Science & Technology

journal homepage: www.elsevier.com/locate/jmst

Research Article

Magnetic-dielectric synergistic enhancement effect of anti-perovskite medium-entropy alloy nitride foams designed by lattice expansion engineering

Wangchang Li[a,b,*], Zengbao Ma[a,b], Wanjia Li[a,b], Lun Fan[a], Yue Kang[c], Ting Zou[c], Xiao Han[c], Yao Ying[a,b], Wenbo Xiang[a,b], Zhiwei Li[d], Jing Yu[a,b], Jingwu Zheng[a,b], Liang Qiao[a,b], Juan Li[a,b], Min Wu[a,*], Shenglei Che[a,b,*]

[a] College of Materials Science and Engineering, Zhejiang University of Technology, Hangzhou 310014, China
[b] Research Center of Magnetic and Electronic Materials, Zhejiang University of Technology, Hangzhou 310014, China
[c] Systems Engineering Institute, Beijing 100010, China
[d] School of Physical Science and Technology, Lanzhou University, Lanzhou 730000, China

ARTICLE INFO

Article history:
Received 15 February 2024
Revised 14 March 2024
Accepted 14 March 2024

Keywords:
Medium-entropy alloy nitride foams
Anti-perovskite structure
Lattice expansion Engineering
Magnetic-dielectric synergistic
Electromagnetic wave absorption

ABSTRACT

A single-phase anti-perovskite medium-entropy alloy nitride foams (MEANFs), as innovative materials for electromagnetic wave (EMW) absorption, have been successfully synthesized through the lattice expansion induced by nitrogen doping. This achievement notably overcomes the inherent constraints of conventional metal-based absorbers, including low resonance frequency, high conductivity, and elevated density, for the synergistic advantages provided by multimetallic alloys and foams. Microstructural analysis with comprehensive theoretical calculations provides in-depth insights into the formation mechanism, electronic structure, and magnetic moment of MEANFs. Furthermore, deliberate component design along with the foam structure proves to be an effective strategy for enhancing impedance matching and absorption. The results show that the MEANFs exhibit a minimum reflection loss (RL_{min}) value of −60.32 dB and a maximum effective absorption bandwidth (EAB_{max}) of 5.28 GHz at 1.69 mm. This augmentation of energy dissipation in EMW is predominantly attributed to factors such as porous structure, interfacial polarization, defect-induced polarization, and magnetic resonance. This study demonstrates a facile and efficient approach for synthesizing single-phase medium-entropy alloys, emphasizing their potential as materials for electromagnetic wave absorption due to their adjustable magnetic-dielectric properties.

1. Introduction

Nowadays, the rapid development of information technology has led to the extensive use of electronic devices in both military and civilian sectors. As a result, there has been a significant increase in electromagnetic pollution and interference, which has gained considerable attention [1–3]. Consequently, a substantial amount of research has been dedicated to the investigation of electromagnetic wave absorbers, which are capable of effectively absorbing electromagnetic wave energy and converting it into thermal energy. Traditional magnetic alloys are commonly employed by researchers due to their high saturation magnetization and permeability which have shown impressive loss capacity and exceptional dielectric properties [4–6]. However, these types of magnetic alloys possess extremely high electrical conductivity, and it is difficult to achieve optimal impedance matching due to the skin effect where the incident electromagnetic waves cannot penetrate the alloy but are strongly reflected on the surface. Moreover, the inferior corrosion resistance results in a gradual decline in the electromagnetic wave dissipation capability of magnetic alloys over time. These drawbacks pose substantial obstacles to the research and application of magnetic alloy materials as highly efficient electromagnetic wave absorbers [7].

In contrast, medium-entropy alloys refer to solid solutions composed of three to four primary metals that significantly distort the crystal lattice due to imbalances among atom size, mass, and bond state [8]. It offers the advantages of low-entropy alloys, such as high saturation magnetization and permeability, while concurrently reducing the electrical conductivity. Moreover, the incorporation of elements such as copper effectively reduces the oxida-

* Corresponding authors.
E-mail addresses: wcli@zjut.edu.cn (W. Li), wum@zjut.edu.cn (M. Wu), cheshenglei@zjut.edu.cn (S. Che).

https://doi.org/10.1016/j.jmst.2024.03.067
1005-0302/

tion rate of ferromagnetic alloys [9]. Therefore, the exploration of high/medium entropy magnetic alloys, which display robust capabilities for electromagnetic wave dissipation, has emerged as a prominent area of research.

Nonetheless, the fusion of distinct metallic components may induce phase separation and give rise to non-uniform structures, decreasing in configurational entropy (ΔS_{conf}) defined as Eq. (1) [10,11], which poses a substantial challenge in material fabrication [12].

$$S_{config} = -R\left[\left(\sum_{i=1}^{N} x_i \ln x_i\right)_{cation-site} + \left(\sum_{j=1}^{M} x_j \ln x_j\right)_{anion-site}\right] \quad (1)$$

where R, $N(M)$, and $x_i(x_j)$ refer to the gas constant, atomic species, and contents at the cation (anion) sites, respectively.

Relevant studies have indicated that the introduction of boron, nitrogen, sulfur, phosphorus, and other elements can effectively induce alterations in the microstructure and facilitate the phase transition of the material [13–15]. However, only a few reports regarding the doping of various non-metallic elements stabilize or promote the formation of single-phase high/medium entropy alloys. In our previous study, N atom doping can promote the volume expansion of matrix phase cells [16,17], which may accommodate more other metal atoms, providing an idea for the preparation of single-phase high/medium entropy alloys. In addition, nitrogen atom doping reduced conductivity and heightened antioxidative properties, enabling the regulation of impedance matching and environmental suitability, thereby improving the stable dissipation capacity of EMW [18]. In addition, another major challenge in the application of high/medium entropy alloys in the field of electromagnetic wave absorption is their high density, which poses a considerable challenge in fulfilling the requirements for a thin, wide, lightweight, and robust absorber.

To overcome this challenge, researchers have explored two main approaches: the design of micro-nano structures and the use of dielectric composite-controlled impedance matching [19,20]. In the former approach, micro/nanostructured metals, such as metal nanochains [21–23], are developed as an alternative to address the high density of bulk metals. Nevertheless, the high surface energy of these structures can lead to agglomeration [21,24,25], which worsens the performance of electromagnetic wave absorption. Additionally, the inferior chemical stability of nano-metals is more susceptible to oxidation when exposed to air [26,27]. In the latter approach, carbon-based materials such as graphene and carbon nanotubes have been extensively applied as lightweight carriers of metal nanoparticles due to their excellent dielectric properties [28,29]. This allows for the protection of metal nanoparticles from oxidation through encapsulation. However, these methods still confront challenges in achieving efficient electromagnetic wave absorption. In conclusion, the suboptimal impedance matching and instability of metallic materials constrain their deployment in efficient electromagnetic wave absorbers. Considering the aforementioned issues, it is feasible to fabricate porous high/medium-entropy alloy structural materials for the development of efficient broadband electromagnetic absorbers. From a structural perspective, high porosity can reduce the weight of the material and enhance its absorbing and scattering properties. Regarding component design, optimizing the proportions of various metal atoms can improve impedance matching and promote the dissipation of electromagnetic waves [30].

Herein, this work fabricated a high microwave absorbing efficient anti-perovskite medium entropy alloy nitride foam designed by lattice expansion engineering. A sol-gel self-propagating method was utilized to synthesize the metal oxide foams, which were subsequently reduced and nitrided to obtain the nitriding foams. Nitrogen atom doping promotes the expansion of the lattice, resulting in a single-phase perovskite crystal structure of medium entropy alloy nitrides. Notably, the porous architecture of the foam facilitates easier penetration and scattering of electromagnetic waves, thereby enhancing its impedance-matching properties. Additionally, defects induced by nitrogen doping enhance electromagnetic wave absorption. The foams demonstrated excellent electromagnetic wave absorption properties, with a minimum reflection loss of −60.32 dB at 4.81 mm and an effective absorption bandwidth of 5.28 GHz at 1.69 mm. Furthermore, the formation mechanism and electromagnetic wave absorption mechanism of MEANFs with single-phase anti-perovskite structure have also been revealed.

2. Experimental

2.1. Materials

Iron nitrate nonahydrate ($Fe(NO_3)_3{\cdot}9H_2O$), nickel nitrate hexahydrate ($Ni(NO_3)_2{\cdot}6H_2O$), and copper nitrate trihydrate ($Cu(NO_3)_2{\cdot}3H_2O$) were all purchased from Sinopharm Chemical Reagent Co. Ltd. (Shanghai, China), cobalt nitrate hexahydrate ($Co(NO_3)_2{\cdot}6H_2O$) and glycine ($C_2H_5NO_2$) were supplied by Macklin Biochemical Co., Ltd., (Shanghai, China). All reagents in this work are of analytical grade. All solutions were freshly prepared with ultrapure water.

2.2. Synthesis of medium-entropy alloy nitride foams

According to the stoichiometric ratio, weigh out a total molar mass of 50 mmol of ferric nitrate nonahydrate, nickel nitrate hexahydrate, copper nitrate trihydrate, and cobalt nitrate hexahydrate dissolved in 25 mL of ultrapure water. After stirring with a magnetic stirrer for 30 min, add 30 mmol of glycine and continue stirring for another 30 min. Heat the resulting homogeneous solution to 200 °C to evaporate the water and form a thick gel until spontaneous combustion occurs. Take the obtained fluffy powder and subject it to reduction at temperatures ranging from 400 to 700 °C with a heating rate of 10 °C/min under an atmosphere containing 25 % N_2 and 75 % H_2 for a duration of 1.5 h to obtain $Fe_xNi_{75-x}Cu_5$ medium-entropy alloy foam. Subsequently, Fe50–0, Fe60–0, and Fe75–0 alloys were subjected to a nitridation treatment within the same temperature range under an atmosphere comprising 75 % N_2 and 25 % NH_3. This process led to the formation of nitride foams derived from medium entropy alloys treated at varying temperatures. Simultaneously, under the same atmosphere and at a temperature of 500 °C all exhibited single-phase formation. The required durations for nitriding were 480, 60, and 25 min for the respective sample groups. Consequently, the resulting samples were denoted as Sample Fe50–480, Fe60–60, and Fe75–25. In addition, all medium-entropy alloys and nitride foams presented in the paper are named in the following way, for samples with different nitride times at the same nitride temperature (500 °C), among which $Fe_{50}Co_{25}Ni_{20}Cu_5$ nitride foams are named Fe50–0, Fe50–15, Fe50–25, Fe50–60, Fe50–240, and Fe50–480. $Fe_{60}Co_{15}Ni_{20}Cu_5$ nitride foam named Fe60–0, Fe60–15, Fe60–25, and Fe60–60. $Fe_{75}Ni_{20}Cu_5$ nitride foams are named Fe75–0, Fe75–15, Fe75–25, and Fe75–60. For the samples with the same nitriding time (25 min) at different nitriding temperatures, $Fe_{50}Co_{25}Ni_{20}Cu_5$ nitride foams are named 400 °C Fe50, 500 °C Fe50, 600 °C Fe50, 650 °C Fe50, and 700 °C Fe50. $Fe_{60}Co_{15}Ni_{20}Cu_5$ nitride foams are named 400 °C Fe60, 500 °C Fe60, 600 °C Fe60, 650 °C Fe60, and 700 °C Fe60. $Fe_{75}Ni_{20}Cu_5$ nitride foams are named 400 °C Fe75, 500 °C Fe75, 600 °C Fe75, 650 °C Fe75, and 700 °C Fe75.

2.3. Characterization

The crystal structure of all samples was characterized by X-ray diffraction (XRD Cu K_α radiation, 40 kV/40 mA). The composition was further confirmed by transmission of Mössbauer spectra with a source of 57Co. X-ray photoelectron spectrometry (XPS, Thermo Scientific K-Alpha) was used to analyze the species and valence of elements of the samples. The microstructure was observed by scanning electron microscopy (SEM, Zeiss-sigma 300) and transmission electron microscope (HRTEM, JEM-2100UHR STEM). The elemental distribution was characterized by an energy-dispersive X-ray detector (EDS). High-resolution high-angle annular dark field (HAADF) scanning TEM (STEM) images and geometric phase analysis (GPA) were analyzed by Gatan digital micrographs software. The static magnetic properties of all samples are measured by a vibrating sample magnetometer (VSM, Lakeshore 7407). The electromagnetic wave absorption property determined by electromagnetic parameters under 2–18 GHz was carried out by vector network analyzer system (VNA, 3672C-S). The sample for measuring electromagnetic parameters was prepared by uniformly blending the medium-entropy alloy and its nitride foam (15 wt% of all samples) with paraffin wax, which was subsequently pressed into a customized coaxial mold featuring an inner diameter of 3.04 mm and an outer diameter of 7.00 mm. Following the principles of transmission line theory, the acquired data were transformed into a computational formula to calculate the reflection loss value.

$$RL = 20\log\left|\frac{Z_{in}-Z_0}{Z_{in}+Z_0}\right| \quad (2)$$

$$Z_{in} = Z_0\sqrt{\frac{\mu_r}{\varepsilon_r}}\tanh\left(j\frac{2\pi fd}{c}\sqrt{\mu_r\varepsilon_r}\right) \quad (3)$$

In these equations, Z_{in} and Z_0 are the input impedance of absorbing materials and the impedance of free space, d is the thickness, c is the speed of light, f is the frequency, ε_r and μ_r are the complex permittivity and permeability, respectively.

2.4. Calculation

All calculations were performed using a first-principles approach based on density functional theory with the Vienna *Ab initio* Simulation Package (VASP) [31]. The influence of the core electrons is replaced by atomic projected augmentation wave (PAW) potentials [32]. The valence electron configurations of $3d^6\ 4s^2$, $3d^7\ 4s^2$, $3d^8\ 4s^2$, $3d^{10}\ 4s^1$, and $2s^2\ 2p^3$ were used for Fe, Co, Ni, Cu, and N atomic potentials, respectively. The Perdew–Burke–Ernzerhof (PBE) exchange-correlation function was used [33]. The wave function is expressed in terms of a plane wave basis set with an energy cutoff of 400 eV. 80-atom supercell structure is used before nitrogen filling, while the alloy structure after nitrogen filling is based on the structure before nitrogen filling with the addition of 20 N atoms to the supercell structure. The number of atoms and the structure ratio structure correspond to $Fe_xNi_{20}Co_{75-x}Cu_5$ (x = 50, 60, 75) and $Fe_xNi_{20}Co_{75-x}Cu_5N_{25}$ (x = 50, 60, 75). For geometric optimization calculations, the Brillouin region was sampled using a 4 × 4 × 4 Gamma-centered central k-point grid. All calculations were performed in a spin-limited manner with an energy convergence criterion of 10^{-5} eV [34]. All internal coordinates were relaxed until the Hermann-Feynman force was less than 0.01 eV/A. The energy convergence criterion of 10^{-5} eV was used to optimize the Brillouin region.

3. Results and discussion

The MEANFs were synthesized by a simple self-combustion method, followed by a reduction and nitridation procedure (Fig. S1 in the Supplementary Material). The gel was vaporized by the solvent and then spontaneously combusts, maintaining sufficient exothermic reaction during this process [35]. This process leads to the release of a large amount of gases, generating porous multimetal oxide-based composite structures (Fig. S2) [36]. The nanostructured gas nitride gel can be obtained by reduction and nitridation treatment. The specific steps for reducing and nitridation are as follows:

$$5Fe_3O_4 + 4NiO + CuO + 25H_2 = Fe_5Ni_4Cu + 10Fe + 25H_2O \quad (4)$$

$$Fe_5Ni_4Cu + 10Fe + NH_3 = \left(Fe_{15}Ni_4Cu\right)_4N + H_2 \quad (5)$$

Initially, at high temperatures, hydrogen diffuses to the surface of the metal oxide foam and undergoes a reduction reaction (Eq. (4)), forming two phases of Fe and Fe_5Ni_4Cu, accompanied by the escape of water vapor. Secondly, metal catalyzes ammonia decomposition to produce a nitriding reaction (Eq. (5)) [15]. N atoms infiltrate the Fe lattice to expand its lattice, inducing lattice expansion, and allowing for the accommodation of more Cu and Ni. In general, the unique structure of the foam enhanced the interface contact between the material and the gas, significantly accelerated the reaction process, and produced a hierarchical and multilevel porous structure in the process of reduction and nitridation. Thus, $(Fe_5Ni_4Cu)_4N$ foam with a single-phase anti-perovskite crystal structure is obtained. The evolution of the crystal structure of $Fe_{75}Ni_{20}Cu_5$ during the nitriding process is illustrated in Fig. 1(a). It undergoes a transition from the body-centered cubic (BCC) lattice of α-Fe and the face-centered cubic (FCC) lattice of Fe_5Ni_4Cu to the face-centered cubic (FCC) lattice of γ'-Fe_4N, exhibiting an anti-perovskite structure.

To reveal the formation mechanism of single-phase medium-entropy alloy nitrides with anti-perovskite crystal structures, medium-entropy alloys with different Fe-Co contents were nitrided at different temperatures and times to monitor their phase transitions. The samples, denoted as $Fe_xCo_{75-x}Ni_{20}Cu_5$, show multiphase structures (Fig. S3). After nitriding for 15 min, it was observed that with an increase in Fe content, the nitrided samples displayed a propensity towards forming a single-phase structure (Fig. S4). Therefore, three samples of $Fe_{50}Co_{25}Ni_{20}Cu_5$, $Fe_{60}Co_{15}Ni_{20}Cu_5$, and $Fe_{75}Ni_{20}Cu_5$ were nitrided at different temperatures and durations for further investigation. As the Fe content decreases, the necessary nitriding time for the formation of a single-phase structure increases, ranging from 25 min for $Fe_{75}Ni_{20}Cu_5$ samples to 480 min for $Fe_{50}Co_{25}Ni_{20}Cu_5$ samples. The corresponding three single-phase samples (Fe75–25, Fe60–60, and Fe50–480) show diffraction peaks at 41.2°, 47.9°, and 70.2°, corresponding to the (111), (200), and (220) crystal faces of γ'-Fe_4N (JCPDS#83-0875) (Fig. 1(b–d)). Additionally, higher nitriding temperatures are required as well. As the Fe content diminishes, the proportion of other metallic elements rises, necessitating a greater driving force (either nitriding temperature or time) to expand the Fe lattice, thereby enabling the accommodation of more alloy constituents and facilitating the formation of a single-phase structure. Nevertheless, with elevated nitriding temperatures, nitrogen atoms tend to escape, rendering the formation of single-phase anti-perovskite medium-entropy alloys more challenging. Consequently, nitrided products at higher temperatures continue to exhibit a multiphase alloy structure (Figs. S5–S7). Hence, medium-entropy alloy nitrides with a single anti-perovskite crystal structure can be obtained only when the nitriding time is adjusted at a suitable temperature. In addition, theoretical calculations of the formation energy of products before and after nitridation indicate that the formation energy of single-phase products after nitridation is lower, which is consistent with our experimental results (Fig. 1(e) and Table S1). Further research on the atomic occupancy information of Fe75–25 samples is benefi-

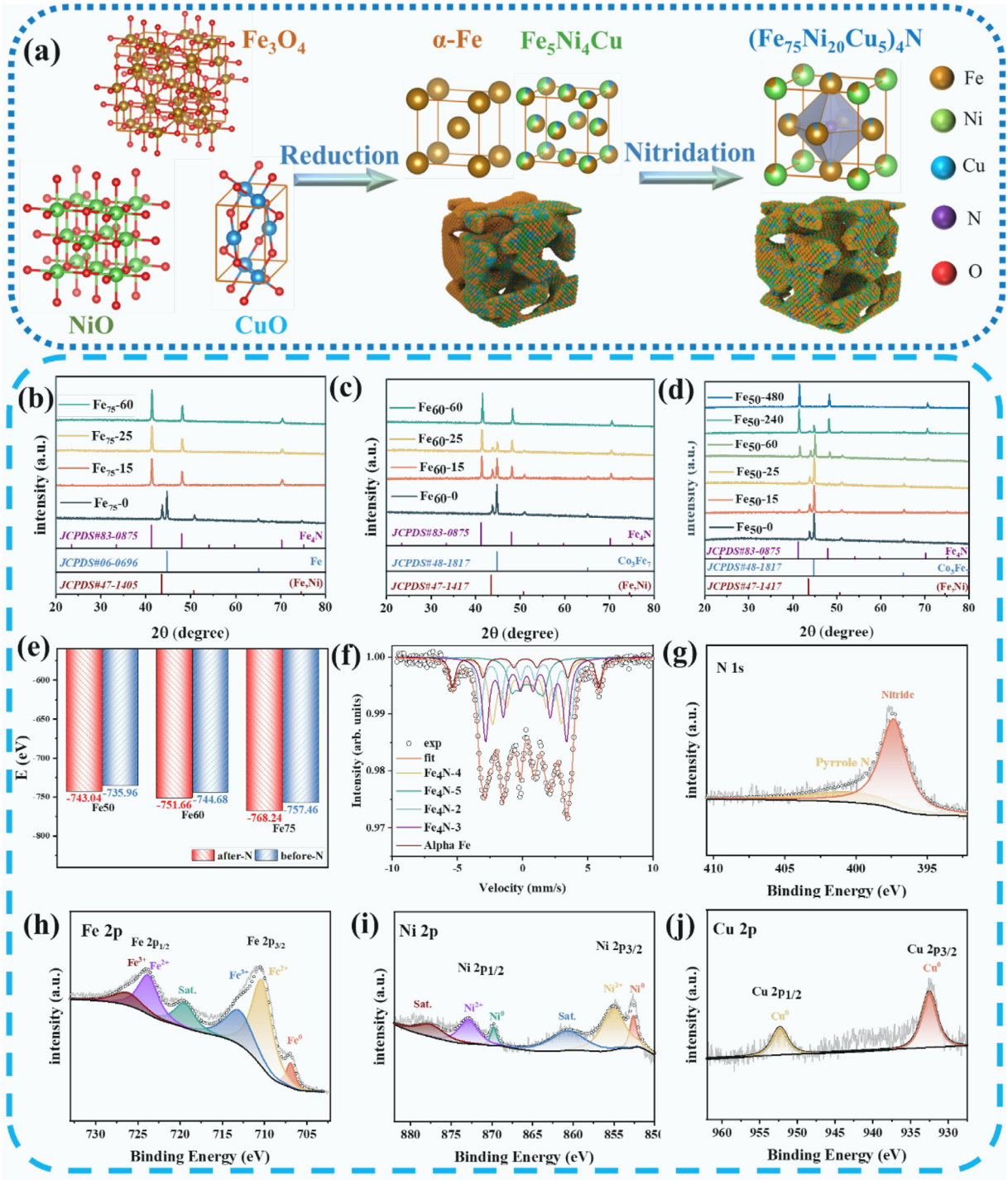

Fig. 1. (a) Schematic diagram of phase transition during nitriding. XRD patterns of MEANFs with different nitriding times, (b) $Fe_{75}Ni_{20}Cu_5$, (c) $Fe_{60}Co_{15}Ni_{20}Cu_5$, and (d) $Fe_{50}Co_{25}Ni_{20}Cu_5$. (e) Theoretical calculation of the formation energy of products before and after nitridation. (f) Mössbauer spectra of Fe75–25. XPS spectra of Fe75–25 (g) N 1s, (h) Fe 2p, (i) Ni 2p, and (j) Cu 2p.

cial for analyzing its crystal microstructure. By analyzing the Mössbauer spectra of typical γ'-Fe_4N (Fig. S8), it is obtained that γ'-Fe_4N exhibits an anti-perovskite structure, which is characterized by N atoms occupying the center of the face-centered cube. In the γ'-Fe_4N lattice, Fe atoms have two distinct types of lattice sites present: corner atoms and face-centered atoms. The corner atoms are surrounded by 12 nearest neighbors and exhibit an atomic environment akin to α-Fe. The face-centered atoms have two nitrogen atoms as their closest neighbors. The proportion between these two atomic configurations is 3:1. However, it is noteworthy that some face-centered Fe atoms usually split into Fe_4N-1 and Fe_4N-2 environments [37,38]. On the basis of the above analysis, the Mössbauer spectra of the typical sample Fe75–25 were tested (Fig. 1(f)). However, the introduction of Ni and Cu atoms has significantly augmented the complexity of the Fe atom environment. Compared to γ'-Fe_4N, the α-Fe occupancy at its corners is merely 5 %, which closely aligns with the Cu content, as indicated in Table S2. This implies that Cu atoms may occupy face-centered positions

while nickel atoms occupy apex positions. Through the integration of Mössbauer spectra and XRD for detailed structural analysis, it is demonstrated that the synthesized sample is a single-phase anti-perovskite medium-entropy alloy nitride. The valence of surface elements and the types of chemical bonds in MENANs were further investigated using XPS analysis. Fig. 1(g–j) illustrates the XPS spectra of Fe75–25, while the N 1s spectrum (Fig. 1(g)) exhibits two distinct peaks at 397.35 and 400.39 eV, corresponding to nitride and pyrrole N, respectively. These peaks primarily indicate that the bonding between nitrogen and metal atoms predominantly occurs in the form of metal nitrides, thereby optimizing the local electronic structure of the material. Additionally, it confirms the presence of a single-phase γ'-Fe_4N [39]. The high-resolution XPS spectrum of Fe in Fig. 1(h) reveals the presence of Fe $2p_{1/2}$ and Fe $2p_{3/2}$ orbitals. The characteristic peak at 706.91 eV corresponds to the zero-valent state of Fe, while the peaks at 710 and 723.48 eV indicate the presence of Fe^{2+}. Additionally, the peaks observed at 711.89 and 725.37 eV provide further evidence for the existence of Fe^{3+}. By analyzing the Ni 2p spectrum (Fig. 1(i)), we observed three distinct nickel states: Ni, Ni^{2+}, and their corresponding satellite peaks. The binding energies at 855.1 and 872.29 eV are attributed to the Ni $2p_{3/2}$ and Ni $2p_{1/2}$ electrons, while the peaks at 860.78 and 877.61 eV represent satellite features. The remaining peaks correspond to metallic nickel with energies of 852.62 and 869.8 eV [40–42]. By comparing the XPS spectra of Fe75–25 Cu 2p in Fig. 1(j) and Fe75–0 Cu 2p in Fig. S10, it was observed that the oxidation state of Cu is no longer detectable after nitridation, thereby demonstrating the efficacy of nitridation in suppressing material oxidation.

A representative MEANF exhibits lightweight characteristics (Fig. 2(a)) with a low density of approximately 0.028 g/cm^3. SEM morphology analysis and BET (Fig. S15) reveals uniformly distributed finely graded multi-level pores, ranging from tens of nanometers to 2 μm within the material (Fig. 2(b)), which is caused by the gradual consumption of fuel during combustion. These multi-level pores, with a substantial surface area, facilitate the absorption, reflection, and scattering of electromagnetic waves [43,44]. The SEM-EDS dot sweep show that the proportion of elements in our sample is very close to the feeding ratio (Fig. S16). To elucidate the detailed microstructure of MEANFs in single-phase anti-perovskite crystal structure, Rietveld refinement was used to study the crystallographic information of Fe75–0 and Fe75–25 samples (Fig. 2(d)). The refined crystal parameters of $Fe_{75}Ni_{20}Cu_5$ before and after nitridation for each phase are presented in Table S3. The Fe75–0 sample has a dual-phase structure, comprising the α-Fe phase with a standard BCC structure and the Fe_5Ni_4Cu phase with a standard FCC structure. The unit cell volume of α-Fe is 23.6 Å, whereas the unit cell volume of our nitrogenized sample Fe75–25 is 54.3 Å, indicating a substantial expansion in comparison. In addition, when the N atom enters the α-Fe lattice, the initial cell volume expands to accommodate more other metal atoms, increasing the configurational entropy, leading to a decrease in the Gibbs free energy, and thus stabilizing the crystal structure [45]. The microstructure of Fe75–0 and Fe75–25 samples was further investigated using HRTEM. In the Fe75 sample, two distinct crystal phases were identified (Fig. 2(e–g)). It was observed that the crystal plane with a crystal plane spacing of 1.94 Å corresponds to the (110) crystal plane of BCC lattice iron, associated with a spatial group of *Im*-3*m*. The crystal plane with a crystal plane spacing of 2.15 Å represents the (110) crystal plane of the BCC lattice Fe_5Ni_4Cu, corresponding to a spatial group of *Fm*-3*m*. The TEM-mapping image also shows the segregation of Ni and Cu (Fig. S17). The TEM analysis of the Fe75–25 sample reveals only one crystal phase (Fig. 2(h–k)). The crystal planes with a spacing of 2.63 Å and 3.73 Å correspond to the (110) and (100) crystal planes of $(Fe_{75}Ni_{20}Cu_5)_4N$, featuring an anti-perovskite crystal structure, with a spatial group of *Pm*-3*m*. Additionally, Fig. 2(c, l) shows the uniformly distributed Fe, Ni, Cu, and N elements, indicating that the substance is a single-phase medium entropy alloy nitride. Geometric phase analysis (GPA), as shown in Fig. 2(m, n), reveals that the strain perpendicular to the (110) crystal plane after nitriding, denoted as ε_{yy}, signifies the significant lattice distortion induced by nitrogen atom doping. This distortion leads to lattice expansion and heightened internal stress in the material, thereby facilitating the incorporation of more metal atoms into the crystal cell. This culminates in the formation of an anti-perovskite structured single-phase medium entropy alloy nitride material. This also provides a lateral explanation for the origin of defects observed in TEM images. Fig. 2(o) exhibits multiple Fe75–25 crystal cells after nitridation from different observation directions on the (110) plane. Notably, regions with higher strain correspond to the positions occupied by Ni, Cu, and N atoms.

Before performing the calculations, three supercell structures with compositions of $Fe_xNi_{20}Co_{75-x}Cu_5$ (x = 50, 60, 75) were selected, each comprising 80 atoms (Fig. S19(a–c)). Subsequently, N atoms were introduced into the $Fe_xNi_{20}Co_{75-x}Cu_5N_{25}$ (x = 50, 60, 75) alloy in proportions identical to those of the experimental samples. A total of 20 N atoms were incorporated, resulting in the formation of medium-entropy alloy nitride with crystal structures depicted in Fig. S19(d–f).

In order to study the formation ability and stability of nitrides with anti-perovskite crystal structure, we conducted calculations to determine the formation energy (E) of M_4N compounds (M = Fe, Ni, Co, Cu). The equations used for these calculations are as follows [46]:

$$E_{\text{from}} = E_{\text{total}} - E_{\text{M}} - E_{\text{N}} \tag{6}$$

where E_{total} is the total energy of the structure, E_{M} and E_{N} are the relaxation energies of metals and nitrogen, and M represents Fe, Ni, Co, or Cu. Fig. 3(a) shows the formation energy of these nitrides. All structures exhibit negative formation energy, indicating their exothermic generation process and overall stability. Notably, γ'-Fe_4N exhibits the lowest formation energy of −47.17 eV among the four nitrides implying that it is relatively easier to form and stabilize. The results explain that the higher the Fe content is, the less the driving force is required to form the single reverse perovskite structure.

To gain insight into the electrical properties of medium entropy alloy nitrides, two-dimensional charge density distribution maps of Fe and $(Fe_{75}Ni_{20}Cu_5)_4N$ were further comprehensively simulated (Fig. 3(b, c)). The anti-perovskite crystal structure of iron-based nitrides, characterized by M-N covalent bonds, induces electron localization, resulting in impedance to charge transfer. Therefore, its resistivity can be readily modulated, thereby facilitating subsequent adjustments to electromagnetic parameters.

Furthermore, the energy band structure and density of states for MEANFs ($Fe_xNi_{20}Co_{75-x}Cu_5N_{25}$ (x = 50, 60, 75)) were calculated. These structures extend along the highly symmetric direction of G-X-S-Y-G-Z-U-R-T-Z|X-U|-T|S-R as shown in Fig. 3(d–f). All spin energy bands overlap with the Fermi level (EF), indicating the presence of metallicity. Meanwhile, the spin band intersects with multiple points on the Fermi level line in different directions, indicating that the nitride has bulk metal properties. In addition, it was observed that the density of states of Fe atoms exhibits asymmetry relative to the energy axis, indicating a ferromagnetic spin order related to the magnetic moment carried by Fe atoms. These findings strongly indicate the presence of ferromagnetism in this alloy. It is evident that the fractional density of states related to Fe has a more significant impact on the overall density of states compared to other atoms, as an increase in Fe content leads to a higher peak density of states in the alloy (Fig. 3(g, h), S20, and S21). This effect is particularly prominent in Fig. 3(g), where the density of states

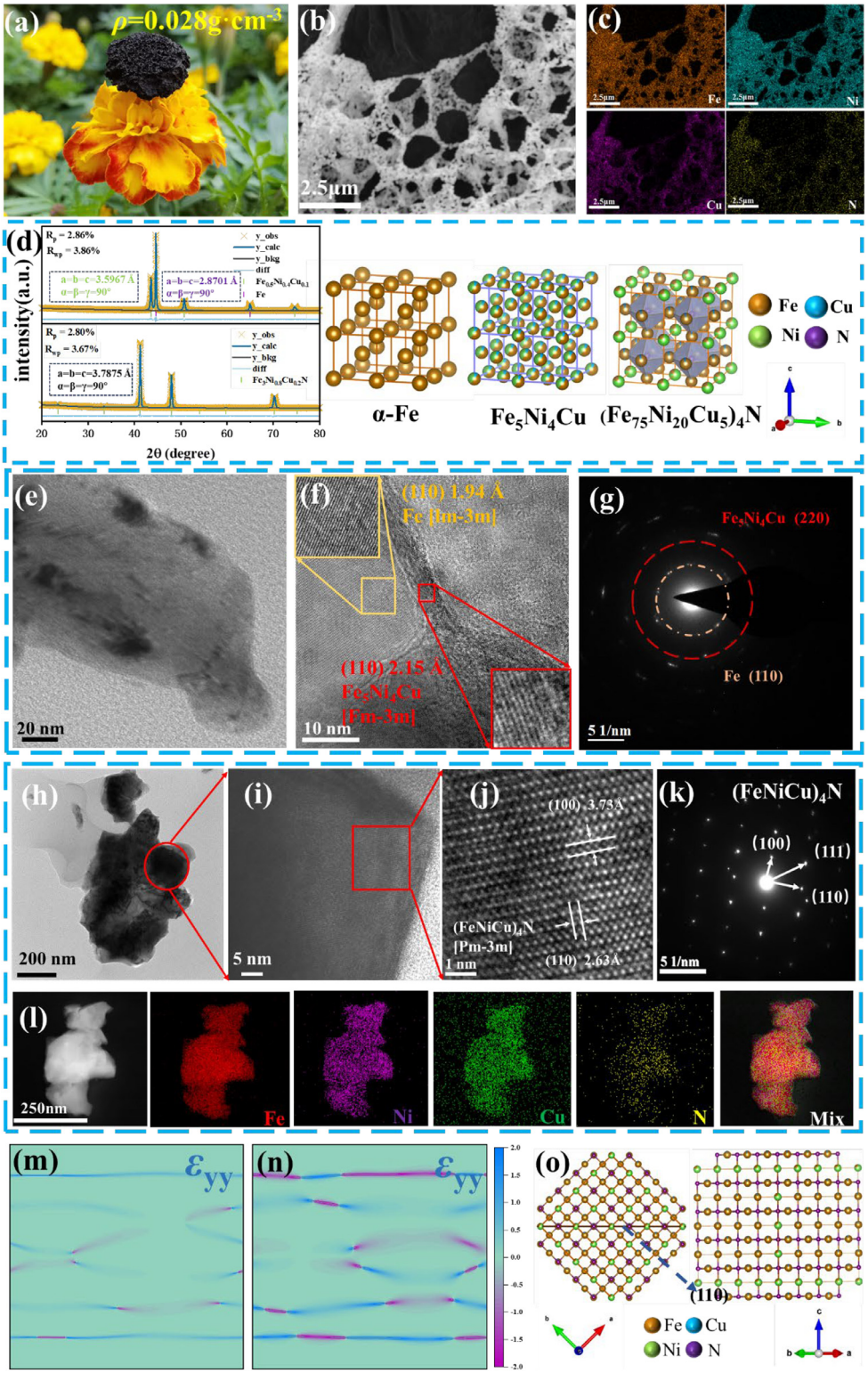

Fig. 2. (a) Digital image for lightweight MEANFs. (b, c) SEM and EDS mapping images of Fe75–25. (d) Rietveld refinement of the Fe75–0 and Fe75–25. (e) TEM and (f) HRTEM images of Fe75–0, (g) corresponding SAED image. (h) TEM and (i, j) HRTEM images of Fe75–25, (k) corresponding SAED image, (l) corresponding EDS mapping. GPA image of Fe75: (m) before nitriding and (n) after nitriding. (o) The (110) surface of the Fe75–25 crystal structure from different perspectives.

of Fe75 is significantly higher than the other two alloys. Therefore, it can be inferred that increasing the Fe content increases the conductivity of the alloy. In contrast, as shown in Fig. S22, all alloys exhibit a decrease in peak density of states after nitriding, with Fe75 showing the most significant decrease. These findings indicate that nitrogen doping reduces the conductivity of the alloy. The magnetic moment of these alloys is influenced by Fe, Ni, and Co, with Fe having the most significant impact. This phenomenon stems from the main contribution of *d*-orbital electrons to the total magnetic moment in these alloys, with Fe playing a crucial role

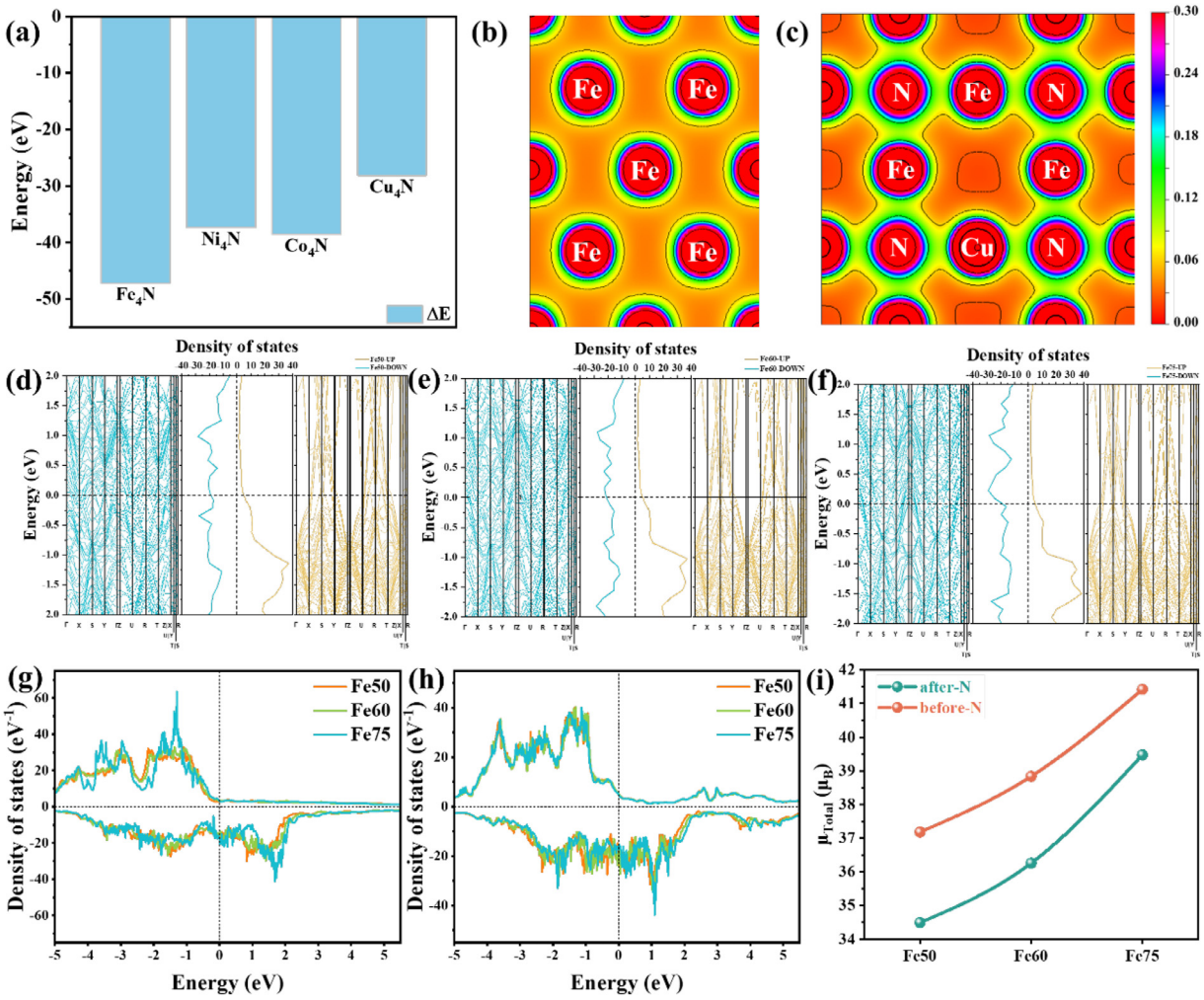

Fig. 3. (a) Formation energy of M_4N (M = Fe, Ni, Co, and Cu). 2D charge density distribution of (b) pure iron, (c) $(Fe_{75}Ni_{20}Cu_5)_4N$. (d–f) The energy band structure diagrams and density of states of $Fe_xNi_{20}Co_{75-x}Cu_5N_{25}$ (x = 50, 60, 75). (g) Total density of states before nitridation. (h) Total density of states after nitridation. (i) Total magnetic moment diagram before and after nitridation.

as the main source of these electrons (Table S4). Therefore, the increase in Fe content leads to an increase in magnetic moment and conductivity within the alloy (Figs. 3(i), S20, and S21).

To investigate the effects of various nitriding processes and Fe/Co content on the magnetic properties of MEANFs, hysteresis loops were analyzed which indicate that all samples exhibit typical ferromagnetism. (Figs. 4(c), S24, and S25). Before nitridation, the saturation magnetization (M_s) initially rises and then declines with increasing Fe content, while the coercivity (H_c) consistently decreases. This is due to the augmentation of magnetic exchange coupling and enhancement of magnetic moment resulting from a certain amount of Co. Consequently, this leads to an improvement in saturation magnetization and a reduction in coercivity.

Further, the study investigated the impact of nitriding at different temperatures on $Fe_{75}Ni_{20}Cu_5$ samples. The findings reveal that at a nitriding temperature of 500 °C, the samples exhibited a lower coercivity of 54.29 Oe and a peak M_s of 119.92 emu/g. In addition, when the nitriding temperature is 600 and 700 °C, H_c is 51.5 and 99.83 Oe, and M_s is 112.15 and 68.57 emu/g, respectively. The deterioration of magnetic properties at higher nitriding temperatures is due to the escape of N atoms, leading to the reformation of the FeNi phase (Fig. S5). Additionally, the Fe75–25 sample, nitrided for 25 min, demonstrated slightly improved magnetic properties compared to the unnitrided Fe75–0 sample. This improvement is likely due to minor oxidation of the unnitrided Fe75–0 sample from air exposure as depicted in the XPS spectra (Fig. S10). Furthermore, the M_s for the Fe60–60 and Fe50–480 samples were 99.29 and 97.22 emu/g, respectively, with corresponding H_c of 53.11 and 52.65 Oe. The study notes that an increase in nitrogen content within the sample, resulting from prolonged nitriding, adversely affects magnetic properties, despite both exhibiting a single-phase anti-perovskite crystal structure [17]. Overall, the Fe75–25 sample exhibits the most favorable magnetic performance, serving as a promising basis for further research into electromagnetic wave dissipation applications.

The complex permittivity ($\varepsilon_r = \varepsilon' - j\varepsilon''$) and complex permeability ($\mu_r = \mu' - j\mu''$) have been obtained to investigate the electromagnetic wave absorption performance and attenuation mechanism of MEANFs. Further, the reflection loss profile of the material has been calculated using transmission line theory [47,48]. In the samples nitrided for 15 min, an initial rise followed by a subsequent decline in the real dielectric constant was observed with the increase in Fe content (Fig. S23(a)). The imaginary dielectric constant often represents the dissipation of energy. The initial increase in the imaginary dielectric constant of the material can be attributed to the multiphase structure of the materials, which would induce interfacial polarization and defect dipole polarization. Then, the subsequent slight decrease of the imaginary dielec-

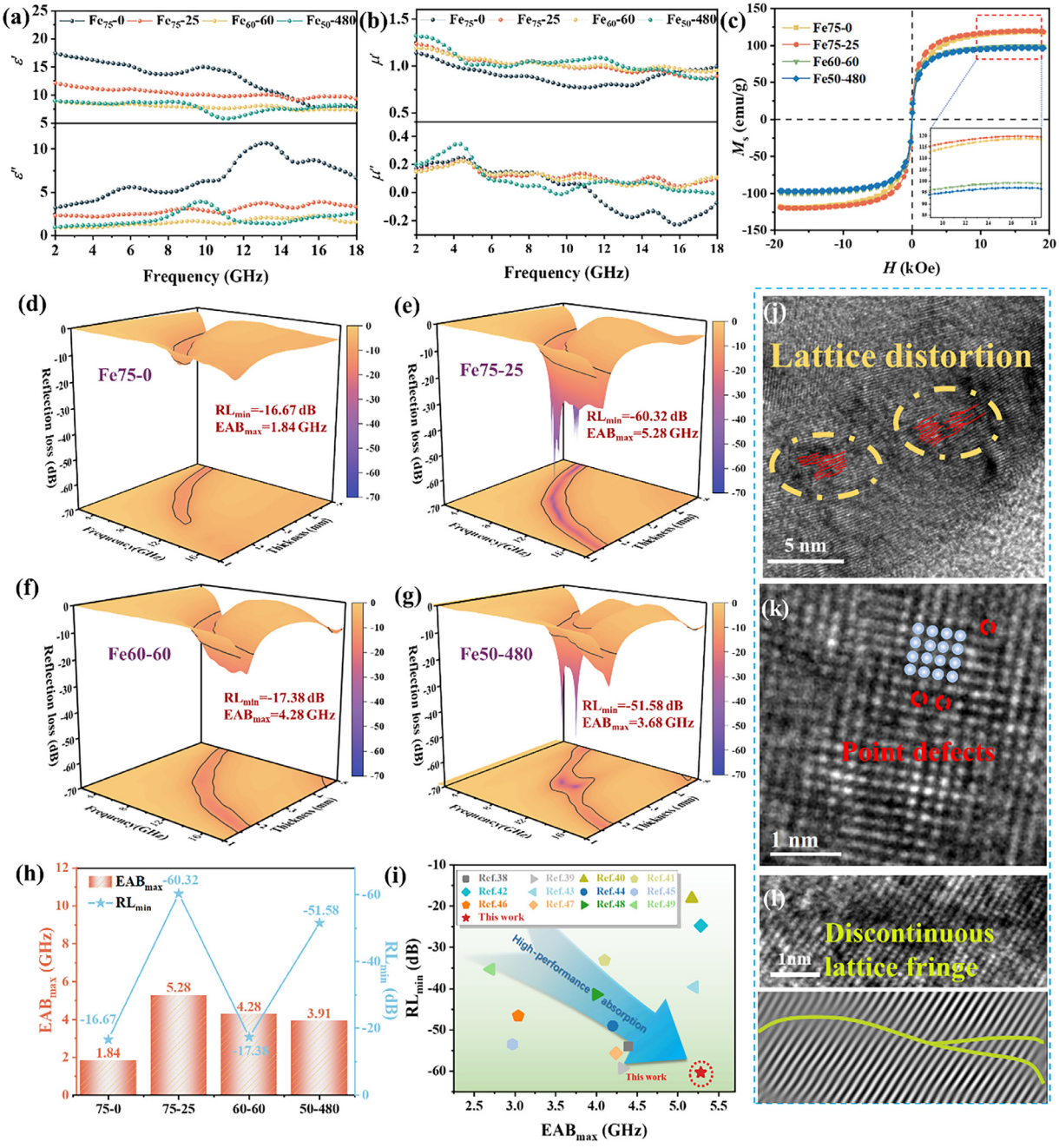

Fig. 4. (a, b) Real part and imaginary part of complex permittivity of Fe75–0, F75–25, Fe60–60, and Fe50–480. (c) VSM of Fe75–0, F75–25, Fe60–60, and Fe50–480. (d–g) 3D plot of RL values vs frequency at different thicknesses and corresponding RL values at given thickness for Fe75–0, F75–25, Fe60–60, and Fe50–480. (h) Summary of widest absorption bandwidth for these samples. (i) Comparison image with previously reported foam or alloy-based electromagnetic wave absorbing materials. (j–l) HRTEM of Fe75–25.

tric constant is attributed to the formation of the anti-perovskite phase, which eliminates certain heterogeneous interfaces. The observed trend in overall permeability is a decline, corresponding to the magnetic properties of the samples. Peaks observed in various frequency bands within the complex permeability spectrum can be attributed to the multimodal magnetic resonance of the magnetic material. (Fig. S23(b)). Due to impedance mismatch, the electromagnetic wave absorption efficiency of this series of samples is low (Fig. S23(c–i)). In addition, electromagnetic parameters of the single-phase anti-perovskite structures with various Fe contents have been further analyzed as shown in Fig. 4(a, b). Compared with the three single-phase samples after nitriding, Fe75–0 has a higher complex permittivity, and the real part of its permittivity shows a strong frequency dependence, which decreases rapidly with the increase of frequency, while the single-phase sample has a slow decrease with the increase of frequency. The ε' of Fe75–25 decreased from 12.12 to 9.3 in the frequency range of 2–18 GHz, while ε'' increased from 2.18 to 3.89. On the Contrary, magnetic permeability exhibited an opposite behavior. The Fe75–25 sample demonstrated a μ' value of 1.23 at 2 GHz, in contrast to 1.13 of the Fe75–0 sample. At low frequency, this increase of the permeability for the nitrided sample can be primarily attributed to the elevated resistivity of medium-entropy alloy nitrides, which effectively suppress eddy current. Therefore, the absorption performance of the sample at low frequency is mainly affected by the magnetic resonance. Moreover, the permeability decreases slowly

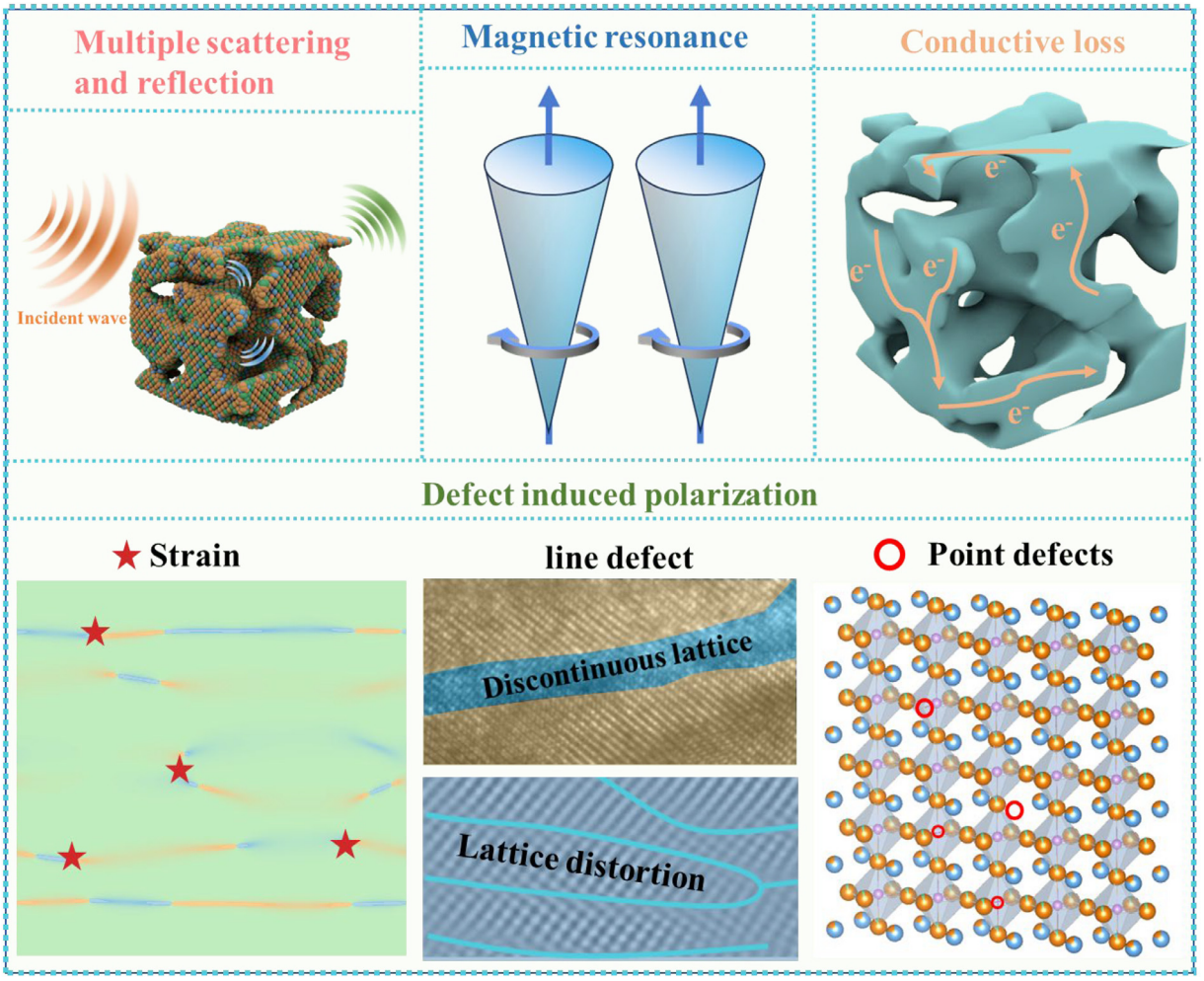

Fig. 5. Schematic diagrams of the main EMW absorption mechanisms for $(Fe_{75}Ni_{20}Cu_5)_4N$ foam absorbing material.

at high frequencies, which also can be ascribed to the high resistivity. It is also noteworthy that the dielectric constant continuously decreases with a slight increase in permeability as the Fe content decreases and the nitriding duration increases for the increase in resistivity. The reflectivity of samples with various thicknesses through electromagnetic parameters is calculated as shown in Fig. 4(d–h). The RL_{min} of Fe75–0, Fe75–25, Fe60–60, and Fe50–480 is −16.67, −60.32, −17.38, and −51.58 dB, respectively. In addition, the EAB_{max} of the above samples are 1.84, 5.28, 4.28, and 3.68 GHz, respectively, with corresponding matching thicknesses of 2.21, 1.69, 1.84, and 3.3 mm. The excellent electromagnetic wave absorption performance of the Fe75–25 sample can be ascribed to the lattice distortion, point defects, and discontinuous lattice stripes in its microscopic crystal structure (Fig. 4(j–l)). Fe75–25 has more Cole-Cole semicircles than Fe75–0 (Fig. S26), indicating that these defects act as polarization centers and induce dipole polarization through defects [49], which increases dielectric loss, leading to multiple fluctuations in the tangent of the dielectric loss angle at different frequencies (Fig. S27).

The loss can be further elucidated by the tangent value of the magnetic loss angle and eddy current loss curve (C_0–f). As depicted in Fig. S27(b), the presence of multiple resonance peaks suggests the occurrence of various resonance losses within these materials. Conventionally, a steady C_0 value is indicative of significant eddy current loss [50]. However, the observed fluctuations of the C_0 value across the entire frequency spectrum, as shown in Fig. S27(c), imply that eddy current losses are negligible in MEANFs. In addition, the attenuation constant (α) of the samples can also reflect the dissipation of electromagnetic waves by the material. Although the α value of the samples without nitriding is high (Fig. S27(d)), it is discernible that the nitrided Fe75–25 sample demonstrates enhanced electromagnetic wave absorption owing to its superior impedance matching property (Fig. S28). Overall, the MEANFs developed in this study showcase exceptional electromagnetic wave absorption, even at reduced filling rates, positioning them as pioneering materials in the realm of lightweight, highly efficient microwave absorbers. The comprehensive absorption performance of the material in this study is superior when compared to other microwave-absorbing composite materials examined in recent related studies, as illustrated in Fig. 4(i) and Table S5 [51–62]. These findings indicate promising prospects for further development.

In conclusion, multiphase metal alloys with unique foam structures can be transformed into $(Fe_{75}Ni_{20}Cu_5)_4N$ with single-phase anti-perovskite crystal structure by N atom doping induced matrix phase lattice expansion, which can be simply mixed with paraffin to obtain excellent EMW performance. Compared with traditional high entropy/medium entropy alloys, N atom-induced matrix phase lattice expansion can accommodate more metal atoms and easily achieve high entropy. In addition, the N atom doping process is simple and can effectively improve the impedance matching of composite materials. Especially, the microstructure of medium-entropy alloy nitrides can be customized through the occupation of metal elements in the matrix phase, resulting in a medium-entropy alloy phase with adjustable electromagnetic

properties due to the synergistic effect of different metal elements. The predominant factors that determine the excellent EMW absorption performance of MEANF composites are as follows: i) The foam structure with evenly distributed hierarchical multi-level pores can increase the reflection and scattering of electromagnetic waves, and promote electromagnetic attenuation and energy conversion. In addition, there are many conductive networks and charge transfer pathways in MEANF composites with large specific surface areas. ii) The doping of nitrogen atoms leads to significant changes in their electronic structure, improving the impedance matching of composite materials, increasing internal stress, generating point defects, discontinuous lattice, and lattice distortion, and enhancing their dielectric loss ability. iii) MEANFs with ferromagnetism can efficiently dissipate electromagnetic waves through magnetic resonance mode. Therefore, MEANFs can achieve excellent EMW absorption performance through excellent impedance matching and magnetic dielectric synergistic loss effects (Fig. 5).

4. Conclusion

MEANFs with a single-phase anti-perovskite crystal structure have been successfully constructed by inducing matrix phase volume expansion through N atom doping. The formation mechanism of the MEANFs with the single-phase anti-perovskite structure has been analyzed through microstructure evolution. The results indicate that doping with N atoms increases the cell volume, leading to an increase in lattice stress, lattice distortion, and the appearance of discontinuous lattices, which increases dielectric loss. Meanwhile, the magnetic resonance losses originating from magnetic components jointly promote the dissipation of electromagnetic waves. For Fe75–25 samples, the RL_{min} reached −60.32 dB at a thickness of 4.81 mm, and the effective absorption bandwidth reached 5.28 GHz at an ultra-thin thickness of 1.69 mm. Furthermore, through the manipulation of N doping and various metal elements, a hierarchical multistage pore structure has been established within the foam framework, encompassing large pores with a diameter of approximately 2 μm and mesoporous pores measuring around 20 nm in diameter. Additionally, the metal nitride foam material exhibits a density of about 0.028 g/cm^3, significantly lower than conventional metal absorbers, thereby meeting the lightweight material criteria for absorptive applications. Therefore, this work provides a straightforward and efficient method for the synthesis of medium-entropy alloys in the inverse perovskite structure, showcasing their high-performance characteristics in broadband.

Declaration of competing interest

The authors declare that they have no known competing financial interests or personal relationships that could have appeared to influence the work reported in this paper.

Acknowledgements

This work was supported by the National Natural Science Foundation of China (Grant No. 52071294), the National Key Research and Development Program (Grant No. 2022YFE0109800), and the Natural Science Foundation of Zhejiang Province (Grant No. LY20E020015).

Supplementary materials

Supplementary material associated with this article can be found, in the online version, at doi:10.1016/j.jmst.2024.03.067.

References

[1] M. Qin, L. Zhang, H. Wu, Adv. Sci. 9 (2022) 2105553.
[2] X. Zhong, M. He, C. Zhang, Y. Guo, J. Hu, J. Gu, Adv. Funct. Mater. 34 (2024) 2313544.
[3] D. Lan, H. Li, M. Wang, Y. Ren, J. Zhang, M. Zhang, L. Ouyang, J. Tang, Y. Wang, Mater. Res. Bull. 171 (2024) 112630.
[4] H.X. Zhang, C. Shi, Z.R. Jia, X.H. Liu, B.H. Xu, D.D. Zhang, G.L. Wu, J. Colloid Interface Sci. 584 (2021) 382–394.
[5] M. He, J. Hu, H. Yan, X. Zhong, Y. Zhang, P. Liu, J. Kong, J. Gu, Adv. Funct. Mater. (2024) 2316691, doi:10.1002/adfm.202316691.
[6] X.L. Cao, Z.R. Jia, D.Q. Hu, G.L. Wu, Adv. Compos. Hybrid Mater. 5 (2022) 1030–1043.
[7] M. Qin, L. Zhang, X. Zhao, H. Wu, Adv. Funct. Mater. 31 (2021) 2103436.
[8] G.M. Tomboc, X. Zhang, S. Choi, D. Kim, L.Y.S. Lee, K. Lee, Adv. Funct. Mater. 32 (2022) 2205142.
[9] J. Dabrowa, G. Cieslak, M. Stygar, K. Mroczka, K. Berent, T. Kulik, M. Danielewski, Intermetallics 84 (2017) 52–61.
[10] A. Sarkar, Q.S. Wang, A. Schiele, M.R. Chellali, S.S. Bhattacharya, D. Wang, T. Brezesinski, H. Hahn, L. Velasco, B. Breitung, Adv. Mater. 31 (2019) 1806236.
[11] B.B. Yang, Y. Zhang, H. Pan, W.L. Si, Q.H. Zhang, Z.H. Shen, Y. Yu, S. Lan, F.Q. Meng, Y.Q. Liu, H.B. Huang, J.Q. He, L. Gu, S.J. Zhang, L.Q. Chen, J. Zhu, C.W. Nan, Y.H. Lin, Nat. Mater. 21 (2022) 1074–1080.
[12] G. Han, M. Li, H. Liu, W. Zhang, L. He, F. Tian, Y. Liu, Y. Yu, W. Yang, S. Guo, Adv. Mater. 34 (2022) 2202943.
[13] Z. Zhou, D. Lan, J. Ren, Y. Cheng, Z. Jia, G. Wu, P. Yin, J. Mater. Sci. Technol. 185 (2024) 165–173.
[14] J. Liu, L. Zhang, H. Wu, Adv. Funct. Mater. 32 (2022) 2110496.
[15] W. Wang, K. Nan, H. Zheng, Q. Li, Y. Wang, J. Mater. Sci. Technol. 181 (2024) 104–114.
[16] W.J. Li, W.C. Li, J.L. Chen, Y. Ying, J. Yu, J.W. Zheng, L. Qiao, J. Li, S.L. Che, J. Alloy. Compd. 928 (2022) 167201.
[17] W.J. Li, W.C. Li, Y. Ying, J. Yu, J.W. Zheng, L. Qiao, J. Li, S.L. Che, J. Mater. Sci. Technol. 175 (2024) 212–222.
[18] W. Li, W. Li, Y. Ying, J. Yu, J. Zheng, L. Qiao, J. Li, S. Che, J. Mater. Sci. Technol. 132 (2023) 90–99.
[19] H.L. Lv, Z.H. Yang, S.J.H. Ong, C. Wei, H.B. Liao, S.B. Xi, Y.H. Du, G.B. Ji, Z.C.J. Xu, Adv. Funct. Mater. 29 (2019) 1900163.
[20] Q.H. Liu, X.H. Xu, W.X. Xia, R.C. Che, C. Chen, Q. Cao, J.G. He, Nanoscale 7 (2015) 1736–1743.
[21] J.J. Patil, W.H. Chae, A. Trebach, K.J. Carter, E. Lee, T. Sannicolo, J.C. Grossman, Adv. Mater. 33 (2021) 2004356.
[22] F. Pan, Y.P. Rao, D. Batalu, L. Cai, Y.Y. Dong, X.J. Zhu, Y.Y. Shi, Z. Shi, Y.W. Liu, W. Lu, Nano-Micro Lett. 14 (2022) 140.
[23] Y.X. Han, M.K. He, J.W. Hu, P.B. Liu, Z.W. Liu, Z.L. Ma, W.B. Ju, J.W. Gu, Nano Res. 16 (2023) 1773–1778.
[24] H. Sakai, T. Kanda, H. Shibata, T. Ohkubo, M. Abe, J. Am. Chem. Soc. 128 (2006) 4944–4945.
[25] J.G. Zhang, Y.F. Zhu, H.J. Lin, Y.N. Liu, Y. Zhang, S.Y. Li, Z.L. Ma, L.Q. Li, Adv. Mater. 29 (2017) 1700760.
[26] C.B. Gao, F.L. Lyu, Y.D. Yin, Chem. Rev. 121 (2021) 834–881.
[27] X.Q. Liu, J. Iocozzia, Y. Wang, X. Cui, Y.H. Chen, S.Q. Zhao, Z. Li, Z.Q. Lin, Energy Environ. Sci. 10 (2017) 402–434.
[28] Y.Z. Zhao, W. Wang, J.N. Wang, J.J. Zhai, X.Y. Lei, W. Zhao, J.N. Li, H.W. Yang, J.X. Tian, J.F. Yan, Carbon 173 (2021) 1059–1072.
[29] B. Zhao, Y. Li, H.Y. Ji, P.W. Bai, S. Wang, B.B. Fan, X.Q. Guo, R. Zhang, Carbon 176 (2021) 411–420.
[30] Q. Chang, H. Liang, B. Shi, H. Wu, Iscience 25 (2022) 103925.
[31] G. Kresse, J. Furthmuller, Comput. Mater. Sci. 6 (1996) 15–50.
[32] P.E. Blochl, C.J. Forst, J. Schimpl, Bull. Mater. Sci. 26 (2003) 33–41.
[33] J.P. Perdew, K. Burke, M. Ernzerhof, Phys. Rev. Lett. 77 (1996) 3865–3868.
[34] D. Waldron, L. Liu, H. Guo, Nanotechnology 18 (2007) 424026.
[35] A. Feng, D. Lan, J. Liu, G. Wu, Z. Jia, J. Mater. Sci. Technol. 180 (2024) 1–11.
[36] A. Varma, A.S. Mukasyan, A.S. Rogachev, K.V. Manukyan, Chem. Rev. 116 (2016) 14493–14586.
[37] L. Fashen, K. Yong, Z. Rongjie, J. Phys.-Condens. Matter 7 (1995) L235–L238.
[38] V.K. Garg, A.C. Oliveira, R.B. Azevedo, M. Wagener, N. Buske, P.C. Morais, J. Magn. Magn. Mater. 272 (2004) 2326–2327.
[39] R.N. Panda, N.S. Gajbhiye, J. Magn. Magn. Mater. 195 (1999) 396–405.
[40] Z. Wang, J. Ang, B. Zhang, Y. Zhang, X.Y.D. Ma, T. Yan, J. Liu, B. Che, Y. Huang, X. Lu, Appl. Catal. B-Environ. 254 (2019) 26–36.
[41] Q. Liu, S. Cao, Y. Fu, Y. Guo, Y. Qiu, J. Electroanal. Chem. 813 (2018) 52–57.
[42] J. Ouyang, Z. He, Y. Zhang, H. Yang, Q. Zhao, ACS Appl. Mater. Interfaces 11 (2019) 39304–39314.
[43] B. Zhan, Y. Hao, X. Qi, Y. Qu, J. Ding, J.-L. Yang, X. Gong, Y. Chen, Q. Peng, W. Zhong, Nano Res. 17 (2023) 927–938.
[44] J. Xiao, B. Zhan, M. He, X. Qi, X. Gong, J.-L. Yang, Y. Qu, J. Ding, W. Zhong, J. Gu, Adv. Funct. Mater. 33 (2023) 2316722.
[45] B.B. Jiang, Y. Yu, J. Cui, X.X. Liu, L. Xie, J.C. Liao, Q.H. Zhang, Y. Huang, S.C. Ning, B.H. Jia, B. Zhu, S.Q. Bai, L.D. Chen, S.J. Pennycook, J.Q. He, Science 371 (2021) 830–834.
[46] R. Zheng, L. Zheng, M. Yang, J. Chem. Phys. 150 (2019) 164301.
[47] J. Liu, L. Zhang, H. Wu, Adv. Funct. Mater. 32 (2022) 2200544.
[48] C.P. Li, L. Zhang, S. Zhang, Q.Q. Yu, D. Li, L. Zhang, C.H. Gong, J.W. Zhang, Nano Res. 17 (2023) 1666–1675.

[49] Y. Pan, D. Lan, Z. Jia, A. Feng, X. Feng, G. Wu, P. Yin, Adv. Compos. Hybrid Mater. 7 (2024) 40.
[50] C.H. Wei, L.Z. Shi, M.Q. Li, M.K. He, M.J. Li, X.R. Jing, P.B. Liu, J.W. Gu, J. Mater. Sci. Technol. 175 (2024) 194–203.
[51] P. Yi, Z. Yao, J. Zhou, B. Wei, L. Lei, R. Tan, H. Fan, Nanoscale 13 (2021) 3119–3135.
[52] X. Cui, X. Liang, J. Chen, W. Gu, G. Ji, Y. Du, Carbon 156 (2020) 49–57.
[53] J. Tao, J. Zhou, Z. Yao, Z. Jiao, B. Wei, R. Tan, Z. Li, Carbon 172 (2021) 542–555.
[54] Y. Shen, Y. Wei, J. Li, Q. Li, J. Ma, P. Wang, B. Li, W. He, X. Du, J. Mater. Sci.: Mater. Electron. 30 (2019) 3365–3377.
[55] R. Guo, D. Su, F. Chen, Y. Cheng, X. Wang, R. Gong, H. Luo, ACS Appl. Mater. Interfaces 14 (2022) 3084–3094.
[56] H. Sun, S.-Q. Yi, N. Li, K.-K. Zou, J. Li, L. Xu, Y.-Y. Wang, D.-X. Yan, Z.-M. Li, J. Colloid Interface Sci. 649 (2023) 501–509.
[57] L. Luo, X. Yuan, D. Wang, X. Qiu, Nanotechnology 34 (2023) 365703.
[58] S. Deng, J. Jiang, D. Wu, Q. He, Y. Wang, J. Colloid Interface Sci. 650 (2023) 710–718.
[59] B. An, M. Wu, X. Yang, Z. Man, C. Feng, X. Liang, Nanomaterials 13 (2023) 1903.
[60] L. Yan, J. Xiang, Y. Li, H. Zhang, S. Tong, Y. Zhang, K. Zhang, J. Mater. Res. Technol. 24 (2023) 9780–9792.
[61] H. Wu, D. Lan, B. Li, L. Zhang, Y. Fu, Y. Zhang, H. Xing, Compos. Pt. B-Eng. 179 (2019) 107524.
[62] P. Yang, Y. Liu, X. Zhao, J. Cheng, H. Li, Adv. Powder Technol. 27 (2016) 1128–1133.